Research
Civil Engineering—Article

# Image-Aided Analysis of Ballast Particle Movement Along a High-Speed Railway

Xuecheng Bian [a], Wenqing Cai [a], Zheng Luo [a], Chuang Zhao [b,*], Yunmin Chen [a]

[a] Key Laboratory of Soft Soils and Geoenvironmental Engineering, Ministry of Education, Department of Civil Engineering, Zhejiang University, Hangzhou 310058, China
[b] Center for Hypergravity Experimental and Interdisciplinary Research, Zhejiang University, Hangzhou 310058, China

## ARTICLE INFO

## ABSTRACT

As a core infrastructure of high-speed railways, ballast layers constituted by graded crushed stones feature noteworthy particle movement compared with normal railways, which may cause excessive settlement and have detrimental effects on train operation. However, the movement behavior remains ambiguous due to a lack of effective measurement approaches and analytical methods. In this study, an image-aided technique was developed in a full-scale model test using digital cameras and a color-based identification approach. 1274 surface ballast particles were manually dyed by discernible colors to serve as tracers in the test. The movements of the surface ballast particles were tracked using the varied pixels displaying tracers in the photos that were intermittently taken during the test in the perpendicular direction. The movement behavior of ballast particles under different combinations of train speeds and axle loads was quantitatively evaluated. The obtained results indicated that the surface ballast particle movements were slight, mainly concentrated near sleepers under low-speed train loads and greatly amplified and extended to the whole surface when the train speed reached 360 km·h$^{-1}$. Additionally, the development of ballast particle displacement statistically resembled its rotation. Track vibration contributed to the movements of ballast particles, which specifically were driven by vertical acceleration near the track center and horizontal acceleration at the track edge. Furthermore, the development trends of ballast particle movements and track settlement under long-term train loading were similar, and both stabilized at nearly the same time. The track performance, including the vibration characteristics, accumulated settlement and sleeper support stiffness, was determined to be closely related to the direction and distribution of ballast particle flow, which partly deteriorated under high-speed train loads.

## 1. Introduction

Compared with ballastless tracks, ballasted tracks have been widely utilized in low-speed passenger and heavy haul railways due to their lower construction cost. However, with an increase in train speeds, the vibration of ballasted tracks is greatly intensified [1,2], and ballast flight might even occur [3], which has detrimental effects on train operation. Moreover, the ballast layer has been considered the main body of track accumulated settlement, requiring frequent maintenance [4,5]. Since the ballast layer is composed of unbound aggregate materials, ballast particles are prone to movement under train loads, which significantly affects the performance of ballasted tracks [6,7]. However, due to the lack of effective measurement approaches and analytical methods, the real movement behavior of ballast particles has not been well investigated but is still unclear.

Previous studies have adopted the discrete element method to simulate ballast particle movements under train loads. For example, Chen et al. [8] simulated the lateral flow of ballast particles upon cyclic loading by two-ball clumps and discovered that it decreased with increasing horizontal confining pressure. Zhang et al. [9] established a two-dimensional discrete element model; the results indicated that higher train speeds resulted in larger ballast acceleration amplitudes. Bian et al. [10] utilized polyhedral elements to build a ballasted track model and discovered that the principal stress rotation caused by moving train

---

* Corresponding author.
    E-mail address: zhaochuang@zju.edu.cn (C. Zhao).

X. Bian, W. Cai, Z. Luo et al.

loads mobilized higher particle movements than those under stationary cyclic loads, which significantly increased the accumulated settlement. Although the comprehensive moving behavior of ballast particles can be modeled by the discrete element method, the process involving numerous particles, complex shapes, and large loading cycles tends to lead to a time-consuming calculation, and the description of energy dissipation remains a challenge [11].

Laboratory model tests are essential not only for verifying the numerical simulations but also for reflecting the actual service environments of ballasted tracks. Conventional measurements of ballast movements were mainly achieved by installing vibration sensors in the designed physical models. For example, Aikawa [12] adopted sensing stones to measure the three-dimensional (3D) acceleration inside the ballast layer. However, they differed from ballast particles in size and shape, which interfered with the movements of surrounding ballast particles. Liu et al. [13] and Fu et al. [14] monitored the translational acceleration and angular acceleration of ballast particles in box tests under cyclic loading by SmartRock sensors, which had a similar appearance to those of common ballast particles and could wirelessly transmit data. However, only the transient vibrations at the limited prescribed positions where sensors had been placed were recorded. It is still difficult to directly monitor the long-term migrations of numerous ballast particles at the same time under train loading.

Image-aided techniques, such as particle image velocimetry (PIV) and particle tracking velocimetry (PTV), which are able to simultaneously identify many tracked targets and record their motions, have been widely utilized to evaluate the strain localization and shear band of soils in laboratory tests [15,16]. This technique has also been tentatively employed to measure the volume change and shear deformation of ballast specimens in triaxial tests [17,18]. Recent studies have tried to take advantage of the image-aided approach in model tests for ballasted tracks. By photographing the transversal cross-section of the track bed in a transparent test box, ballast displacements upon loading were monitored [19–21]. Via a camera mounted over the track structures, the surface ballast flow was observed and discussed with the change in track performance [22–24]. Nevertheless, in the above measurement methods, neighboring ballast particles were considered a unit for displacement evaluation, which disregarded the discreteness and rotation of ballast particles and were unable to exhibit the real behavior of ballast particles. In addition, in these model tests, only vertical stationary cyclic load or horizontal excitation was applied, which considerably differed from the moving loads and hence made the experimental results unable to accurately reflect the actual ballast particle movements under train passage.

The aim of this study is to disclose the movement behavior of ballast particles by incorporating a novel, image-aided technique into a full-scale model test that can replicate actual moving train loads on ballasted track structures. Almost all surface ballast particles were dyed to act as tracked targets for individual movement evaluation, including particle displacement and rotation. A dynamic test and long-term loading test were designed to investigate the moving characteristics of ballast particles and the performance evolution of ballasted tracks. The horizontal displacement and rotation of each tracked ballast particle from the center to the slope of the ballast layer, the effects of train speed and axle load on the movement behavior of ballast particles and the dynamic responses of the ballast layer are discussed. In addition, the relationships between microscopic ballast particle movements and macroscopic vibration, settlement and stiffness of the ballasted track during long-term loading are explored.

## 2. Full-scale physical model of a ballasted railway

### 2.1. Geometry and materials of the physical model

The full-scale physical model of ballasted railways established in this study is shown in Fig. 1. In a rectangular steel model box with a length, width, and height of 5.50, 15.00, and 6.00 m, respectively, a ballasted track was constructed following the Chinese code for the design of high-speed railways [25]. Per the previous 3D finite element simulation [26], the boundary effects of the built model with limited length on its dynamic responses were proven to be trivial. To further mitigate the boundary effects, a 15 mm thick, smooth latex layer was placed on the inner sides of the steel model box.

The ballasted track consisted of eight 2.60 m long, IIIc-type [25] concrete sleepers with a 0.63 m spacing. Two segmented, CHN60-type rails with a gauge of 1.435 m were fixed on each sleeper by elastic strip, V-type fasteners. As shown in Fig. 1(b), between the sleepers and a pile foundation, from the top down, there was a 0.30 m thick ballast layer, 0.70 m thick subballast layer, and 2.05 m thick embankment, which were constructed by graded crushed stones, graded gravels, and granular soils, respectively. Their grain-size distributions are shown in Fig. 2 [27], and their properties are summarized in Table 1. A geogrid was installed at the interface between the ballast layer and the subballast layer. The slopes of the ballast layer, subballast layer and embankment were 1:1.75, 1:1.5, and 1:1.5, respectively. The pile foundation was modeled by concrete pile caps and water bags, with two granular layers and an intermediate geogrid–sand layer above [28].

The embankment, subballast layer, and ballast layer were separated into 8, 3, and 2 layers, respectively, to be compacted by a tamping machine. After model preparation, the sleeper support stiffness upon static loading was evaluated to be 252 kN·mm$^{-1}$. By controlling the densities and foundation coefficients, named $K_{30}$, of the three layers and the sleeper support stiffness, the compactness of the track structure met the engineering requirements. Hence, this full-scale physical model would have nearly the same dynamic characteristics as an actual and typical ballasted high-speed railway in China.

### 2.2. Sensor arrangement

Various sensors were utilized to record the dynamic responses of the ballasted track under train loads, as shown in Figs. 1(a) and (b). Five vibration velocity sensors and a vibration acceleration sensor were mounted on the surface of the ballast layer to measure the vertical vibration from the track center to the bottom of the ballast slope. Four SmartRock (Strdal Co., China) sensors that had nearly the same dimensions as the real ballast particle were embedded in the ballast layer, 0.15 m below the bottom of Sleeper 5, to observe the 3D acceleration. Four laser displacement sensors were installed at both ends of Sleepers 4 and 5 to measure the vibration and settlement of sleepers. Additionally, to record the settlements at different depths of the substructure, four settlement plates with a square dimension of 0.3 m, each of which was connected with a steel bar, a casing tube and a linear variable differential transformer (LVDT), were placed on the surface of the subballast layer and embankment. To further reduce the boundary effects, almost all the sensors were placed near the middle section in the longitudinal direction. In this case, the dynamic responses of the track system could be well reproduced under high-speed moving train loads.

Furthermore, two cameras (i.e., EOS M50 (Canon, Japan) and NEX-7 (Sony, Japan)) with high resolutions (i.e., 6000 × 3368 pixels and 6000 × 4000 pixels, respectively) were installed over the track with their shooting directions downward, and the photographing
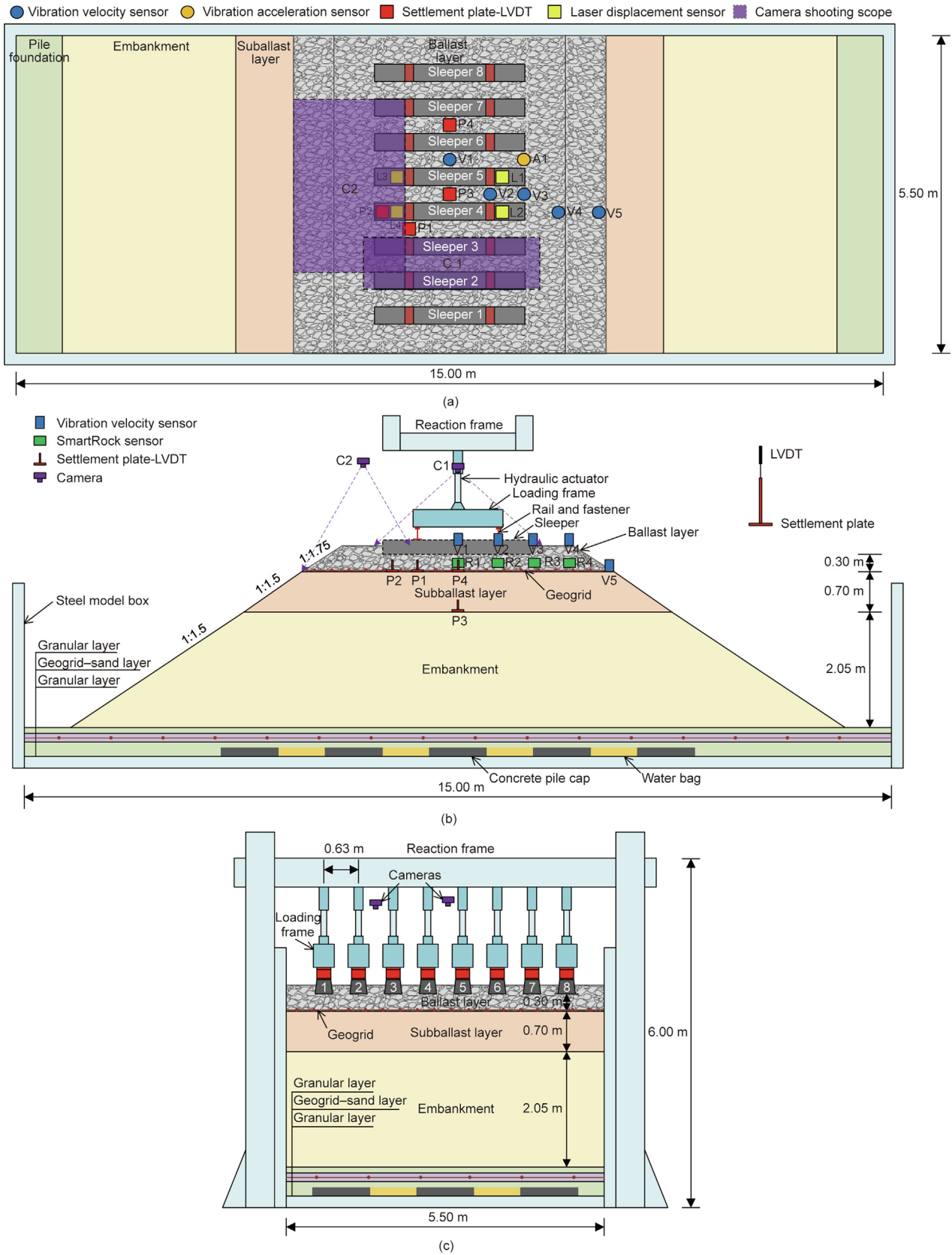
● Vibration velocity sensor  ● Vibration acceleration sensor  ■ Settlement plate-LVDT  ■ Laser displacement sensor  ▦ Camera shooting scope

**Fig. 1.** Geometry of the physical model for ballasted railway and layout of the installed sensors. (a) Top view; (b) transversal cross-section view; (c) longitudinal cross-section view. LVDT: linear variable differential transformer; V: vibration velocity sensor; A: vibration acceleration sensor; P: settlement plate-LVDT; L: laser displacement sensor; C: camera.
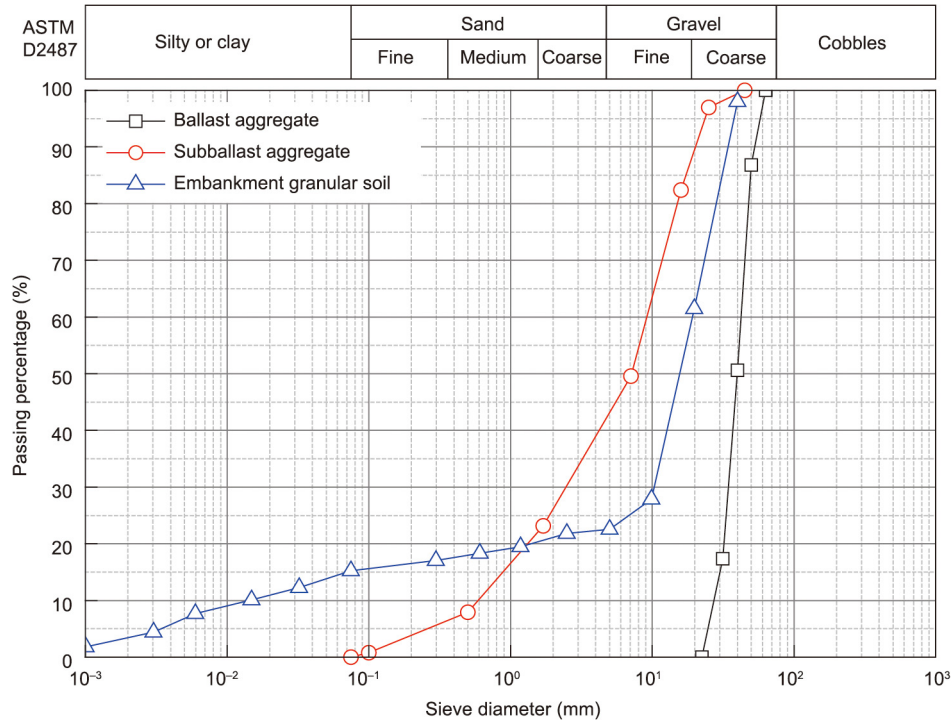
**Fig. 2.** Grain-size distributions of geomaterials in the tested ballasted railway [27].

**Table 1**
Properties of geomaterials in the tested ballasted railway.

| Geomaterial | Water content (%) | Wet density (g·cm$^{-3}$) | Dry density (g·cm$^{-3}$) | Foundation coefficient $K_{30}$ (MPa·m$^{-1}$) |
| --- | --- | --- | --- | --- |
| Ballast aggregate | — | — | 1.865 | 285 |
| Subballast aggregate | 5.5 | 2.278 | 2.159 | 381 |
| Embankment granular soil | 4.2 | 2.027 | 1.945 | 248 |

parameters were predetermined to observe the migration of surface ballast particles between Sleepers 2 and 3 and the outside sleepers. As shown in Fig. 3, these two cameras were fixed on a motionless external frame that was independent of the track structures, and the photos were taken by remote control to avoid any disturbance to the movement measurement. As a result, the cameras could remain stationary with their shooting directions and scopes held constant throughout the loading procedure. Several light emitting diode (LED) lights were also attached to the external frame to gain a bright and constant lighting environment.

### 2.3. Loading system

When a train travels on continuous rails, the moving loads transfer to the underlying track structures through discrete sleepers. Therefore, the dynamic impact of train loads on the railway track can be duplicated by applying equivalent dynamic loads on each sleeper by actuators. Considering the difference between moving train loads and stationary cyclic loads, there should be time intervals $\Delta t$ in the loading curves between two different actuators to simulate the moving effect. For the sake of a simplified description, the loads applied on the eight sleepers for the situation in which a single 170 kN force moves on the rails at a speed ($v$) of 100 km·h$^{-1}$ are shown in Fig. 4(a). The time interval between adjacent sleepers is determined by the moving speed and sleeper spacing. The loading system was established in this way, further

detailed descriptions are provided in previous study [29]. The equivalent dynamic loads on the sleepers were calculated through the dynamic analytical model proposed by Takemiya and Bian [30], according to the parameters of the train, track, and substructure. Verified by *in situ* measurements, previous experiments proved that the testing facility could accurately reproduce the dynamic responses of the actual railway track [31].

The China railway highspeed (CRH) 3-type train was adopted in the test, which features a 25 m long carriage, a bogie spacing of 17.5 m, and an axle spacing of 2.5 m. Fig. 4(b) presents the loads on Sleeper 1 under an eight-carriage train with three different speeds and axle loads, and the other seven sleepers were subjected to loads of the same form but with different intervals per different distances from the first sleeper. To ensure the stability of train loading, an additional constant load of 10 kN was applied to maintain full contact between the loading beam and the rails.

### 2.4. Test procedure

As presented in Table 2, the stages of testing consisted of a dynamic test and long-term loading test. In the dynamic test, the train speed varied from 50 to 360 km·h$^{-1}$, while the axle loads included 17 t for standard carriages and 25 t for heavy haul carriages. These settings covered all the operating trains in China. For convenience, one loading cycle represented the passage of one carriage with four axle loads. Since a multiple-cycle loading
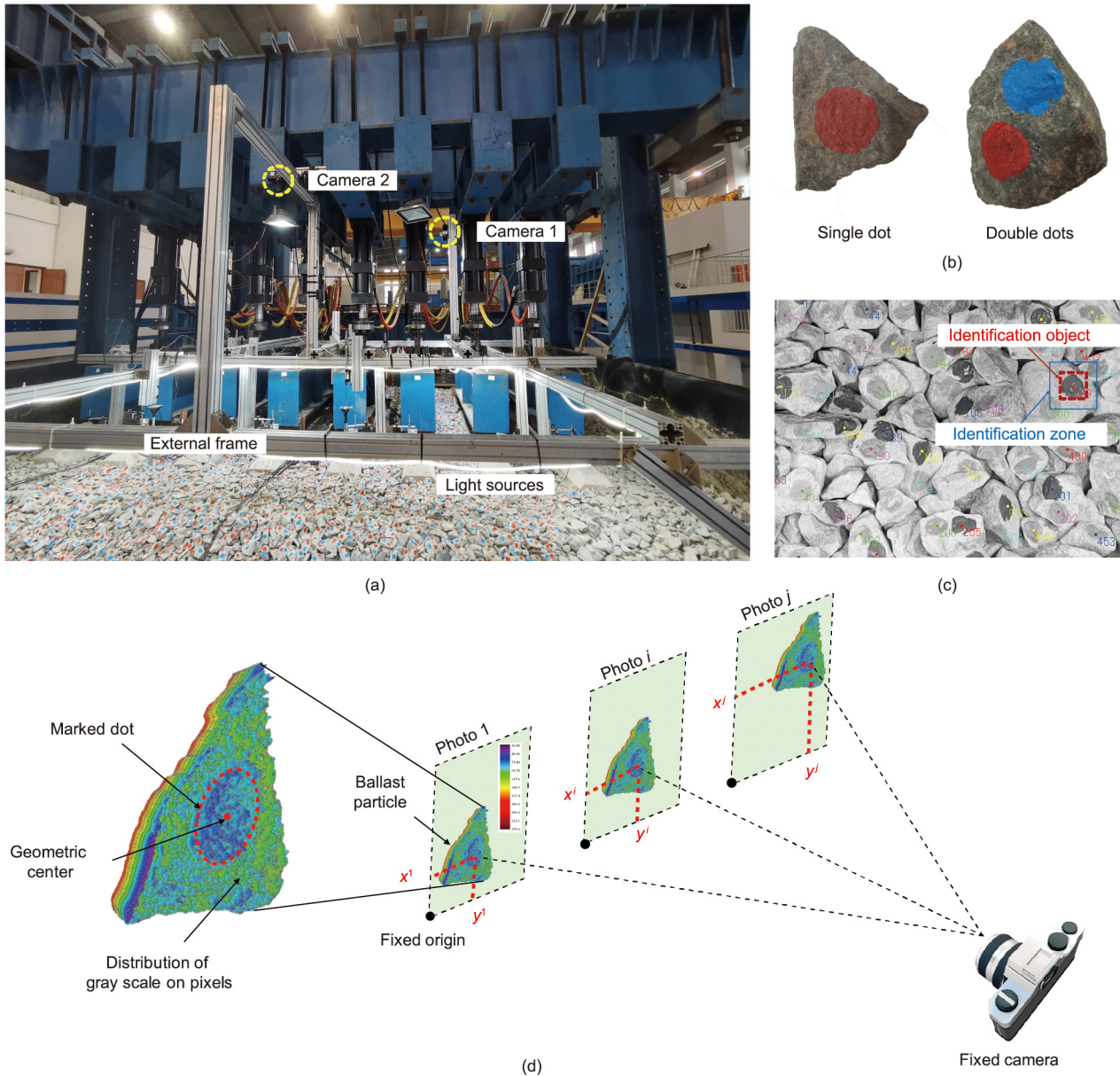
X. Bian, W. Cai, Z. Luo et al.

**Fig. 3.** Image-aided analysis system. (a) Photographing devices; (b) marked ballast particles; (c) tracked target setting; (d) coordinate determination. The variables are defined below.

might cause changes in the stress history of the ballast layer, there were merely 25 carriages passing for each loading case. In the long-term loading test, traffic loads from three typical trains (i.e., ordinary, high-speed, and heavy haul trains) were applied in sequence until the track-accumulated settlement reached the stable state with each load. As listed in Table 2, there was 500 000 carriage loadings during the long-term loading test. Using a normal ballasted railway as an example, there are generally 30 trains in one day, and each train consists of eight carriages. Under such conditions, it would take more than five years to reach the designed number of loading cycles.

## 3. Image-aided technique for ballast movement evaluation

Even though the ballast particles in the photos could be easily recognized, setting artificial tracers could contribute to more precise tracking in subsequent displacement evaluation. Thus, after ballast layer preparation, propylene pigments with two colors were adopted to make circular marked dots with a diameter of approximately 2 cm on the surface ballast particles, as shown in Fig. 3(b). One red dot was dyed for each ballast particle in the observation area, and then some of them were selected for another blue dot with a certain distance from the former red dots. These marked dots acted as tracked targets (tracers) during the dynamic test and long-term loading test.

Photos were taken at the beginning and end of each loading case of the dynamic test and with an interval of 2000-carriage load during the long-term loading test. Since the displacement of ballast particles was limited, a smaller interval would take a longer time for image processing and be meaningless for displacement evaluation. On the other hand, a large interval would miss critical displacement information. Thus, in view of measuring accuracy and operation convenience, the 2000-carriage load was determined to be the photo taking interval during the long-term loading test.

The image-aided technique employed in this study was based on the PTV method, which has been widely employed in hydromechanics. The tracers could be identified by their color, which is
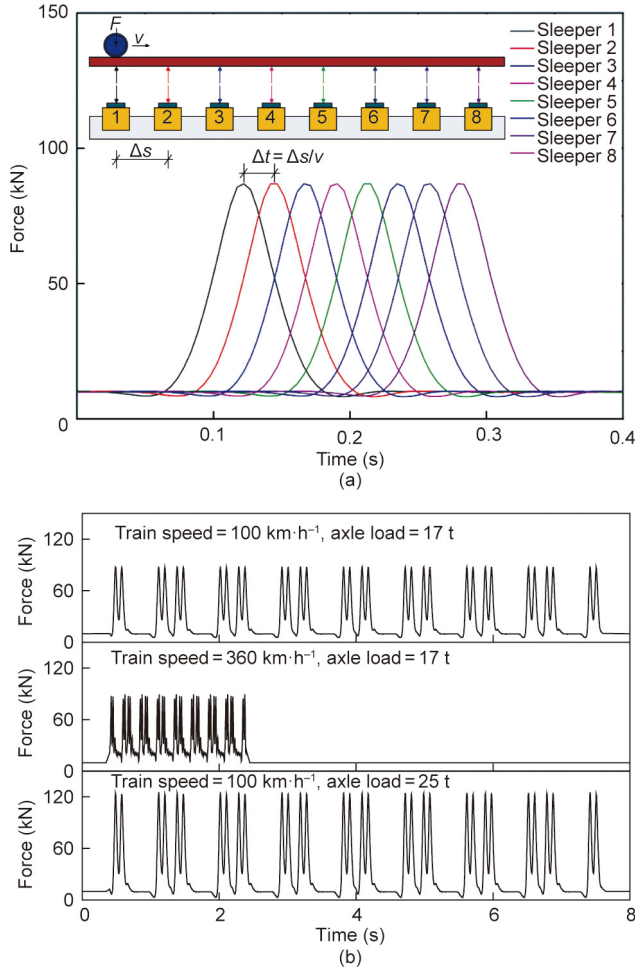
X. Bian, W. Cai, Z. Luo et al.

**Fig. 4.** Time histories of the loading curves of (a) eight actuators for a single moving load ($F$ = 170 kN, $v$ = 100 km·h$^{-1}$) and (b) first actuator for moving loads from an eight-carriage train with three different train speeds and axle loads. $\Delta s$: sleeper spacing.

(38.24 mm) of ballast particles. Moreover, a total of 1274 ballast particles were simultaneously tracked, covering the area from the track center to the bottom of the ballast slope, as indicated in Fig. 1(a). Therefore, the image-aided technique adopted in this study was able to monitor the displacements and rotations of ballast particles in a large scope with a relatively high sensitivity.

In the subsequent image-aided analysis, the procedure of obtaining the displacement and rotation of ballast particles is summarized as follows:

**Step 1**: The origin was set at the track center between Sleepers 2 and 3, which was always fixed throughout the analysis. The lateral and longitudinal directions of the track were set as the $x$-axis and $y$-axis, respectively. After coordinate system setting, the scaling factors between pixels and lengths were determined by the known sleeper size and applied to the displacement evaluation during the analysis. Owing to the fixed camera, constant shooting direction and scope, the coordinate system could also be invariable for all the photos taken by each camera.

**Step 2**: By using the photos taken during the test with the motion capture software (Move-tr/2D; Library Co., Japan), all the marked dots on the ballast particles were set as tracers in the initial photo and were then automatically tracked in the subsequent photos, as shown in Fig. 3(c).

**Step 3**: Since each tracer was displayed by more than a thousand pixels and had a distinguishable grayscale distribution, the coordinate of each marked dot at different moments was determined by identifying its geometric center, as shown in Fig. 3(d). Afterward, based on the obtained coordinate of each marked dot on the ballast particle in different photos, the particle displacement could be quantitatively calculated.

**Step 4**: For a single-dot ballast particle, only its displacement can be obtained. However, if there were two marked dots on one ballast particle, not only its displacement but also the rotation could be further calculated based on the coordinates of these two marked dots. Selecting the double-dot ballast particles as an example, the displacement $d$ and rotation angle $\varphi$ of the $n$th ballast particle from the $i$th moment to the $j$th moment can be expressed as follows.

$$d = \frac{\sqrt{\left(x_{n1}^i - x_{n1}^j\right)^2 + \left(y_{n1}^i - y_{n1}^j\right)^2} + \sqrt{\left(x_{n2}^i - x_{n2}^j\right)^2 + \left(y_{n2}^i - y_{n2}^j\right)^2}}{2} \tag{1}$$

$$\varphi = \arccos\left(\frac{\left(x_{n1}^i - x_{n2}^i\right)\left(x_{n1}^j - x_{n2}^j\right) + \left(y_{n1}^i - y_{n2}^i\right)\left(y_{n1}^j - y_{n2}^j\right)}{\sqrt{\left(x_{n1}^i - x_{n2}^i\right)^2 + \left(y_{n1}^i - y_{n2}^i\right)^2} \times \sqrt{\left(x_{n1}^j - x_{n2}^j\right)^2 + \left(y_{n1}^j - y_{n2}^j\right)^2}}\right) \tag{2}$$

notably different from that of ballast particles. Usually, length measurement is realized through pixel recognition, and the sensitivity of the image-aided technique depends on the actual length related to each pixel [32,33]. As previously introduced, the photos taken during the test by the two cameras had high resolutions. Per the resolutions and shooting scopes of the cameras, the minimum displacement of approximately 0.25 mm could be recognized, which only accounted for 0.65% of the average diameter

**Table 2**
Stages of testing.

| Stage | No. | Train speed (km·h$^{-1}$) | Axle load (t) | Number of loading cycles |
|---|---|---|---|---|
| Dynamic test | 1 | 50 | 17 | 25 |
| | 2 | 100 | 17 | 25 |
| | 3 | 150 | 17 | 25 |
| | 4 | 200 | 17 | 25 |
| | 5 | 250 | 17 | 25 |
| | 6 | 300 | 17 | 25 |
| | 7 | 360 | 17 | 25 |
| | 8 | 100 | 25 | 25 |
| Long-term loading test | 1 | 100 | 17 | 100 000 |
| | 2 | 360 | 17 | 300 000 |
| | 3 | 100 | 25 | 100 000 |

where $(x_{n1}^i, y_{n1}^i)$ and $(x_{n2}^i, y_{n2}^i)$ are the coordinates of the two marked dots on the $n$th ballast particle at the $i$th moment; $(x_{n1}^j, y_{n1}^j)$ and $(x_{n2}^j, y_{n2}^j)$ are those at the $j$th moment; and $i$ or $j$ are the serial numbers of photos taken during the test. In a similar manner, the coordinates of all the tracked dots in the entire photos and ballast particle movements were accordingly evaluated.

Since a fast camera shutter speed was set, the instantaneous state of ballast particles, even with violent movements, could be obtained. As long as the marked dots on the ballast particles were clearly captured in the photos, the image-aided technique adopted in this study was able to accurately track the movements of ballast particles. The failure of particle identification might occur when particles fall over or turn over under high-speed train loads, especially near the slope of the ballast layer. After a 500 000-cycle loading, the error rate of particle identification was determined to be less than 2.2%. If this happened, correction was applied by manually resetting the tracking target. In this manner, the wrong particle identification could be effectively avoided.

## 4. Test results and discussion

### 4.1. Dynamic behavior of ballast layer under train loads

#### 4.1.1. Flow behavior of ballast particles

In the dynamic test, the horizontal movements of surface ballast particles between two sleepers and outside sleepers under train loads (including low-speed, high-speed, and heavy haul train loads) are shown in Figs. 5 and 6, respectively. The arrows indicate the displacement directions of the corresponding ballast particles, while a positive angle indicates counterclockwise rotation. The blue rectangle in Fig. 5 shows the invisible area shaded by a beam of the external frame. Under the train loads with axle loads of 17 t and speeds of 100 km·h$^{-1}$, the ballast particle movements were moderate and mainly concentrated near the sleepers. However, when the train speed increased to 360 km·h$^{-1}$, almost all ballast particle movements were intensified, and the scope of obvious movements expanded to the whole surface, with some particles on the slope sliding downward. For the trains with an axle load of 25 t, the ballast particle movements between two sleepers were similar to those under the 17 t axle load, but the ballast particles far from the sleepers also underwent nonignorable displacements and rotations. Nevertheless, the influence of the axle load on surface ballast particle movements was limited, in contrast with that of the train speed. With the exception of the ballast particles on the slope, which mostly moved outwards, the displacement and rotation directions of other ballast particles were irregular due to the random distribution of the contact forces among them.

To analyze the distribution of ballast particle movements, the ballast layer surface was divided into six horizontal zones, as shown in Fig. 7. Specifically, between Sleepers 2 and 3, Zone 1 was near the center of the sleepers, Zone 2 was near the rail lines, and Zone 3 was near the ends of the sleepers. For the outside sleepers, Zone 4 represented the area within the lateral distance of 40 cm from the sleeper ends, Zone 5 represented the 30 cm wide ballast shoulder with local stacks, and Zone 6 represented the ballast slope. The numbers of tracked ballast particles in the above six zones are shown in Fig. 8. On the whole, the average numbers of single-dot ballast particles and double-dot ballast particles per
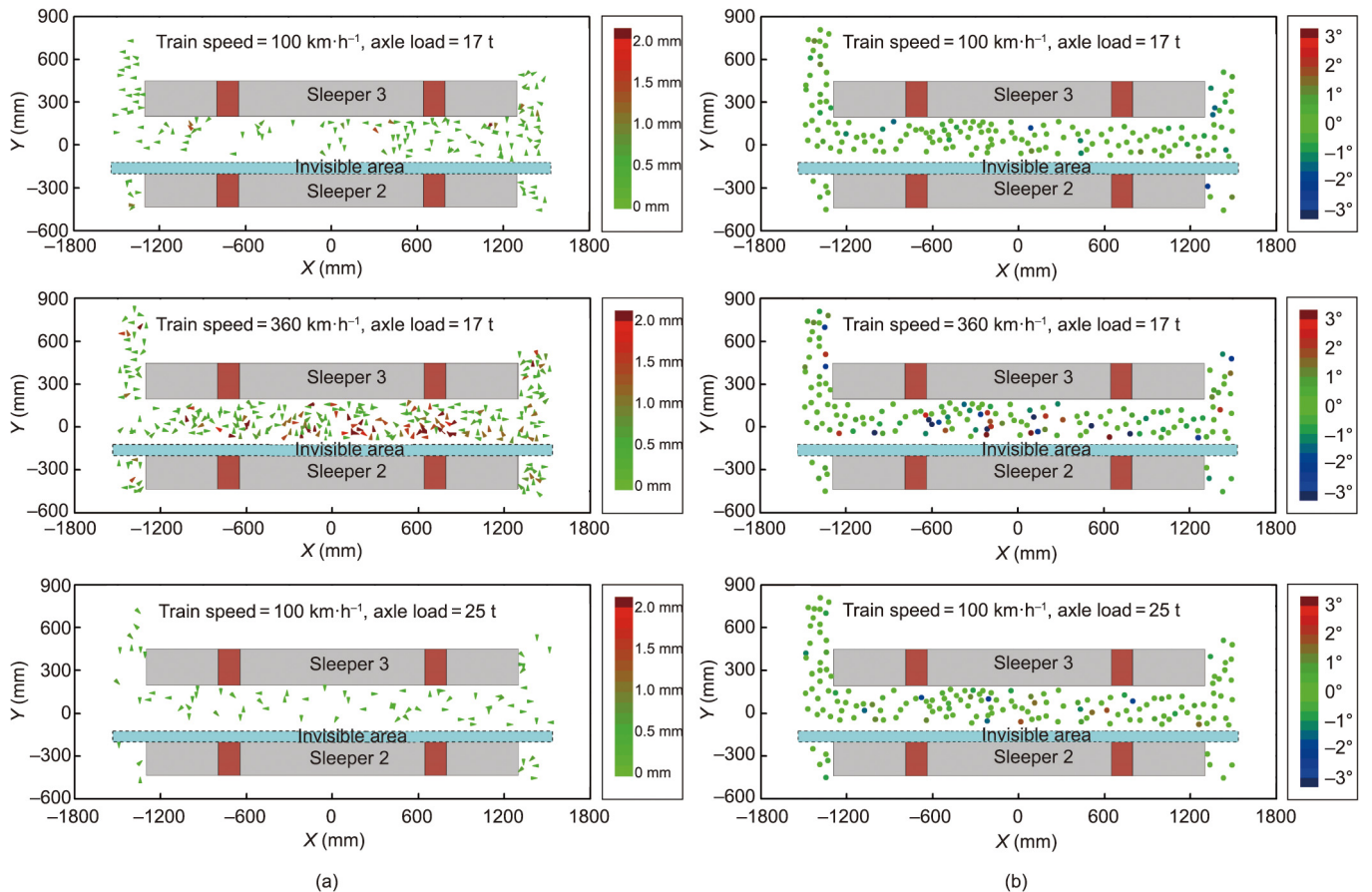


Fig. 5. Movements of surface ballast particles between sleepers in the dynamic test: (a) displacements and (b) rotation angles.
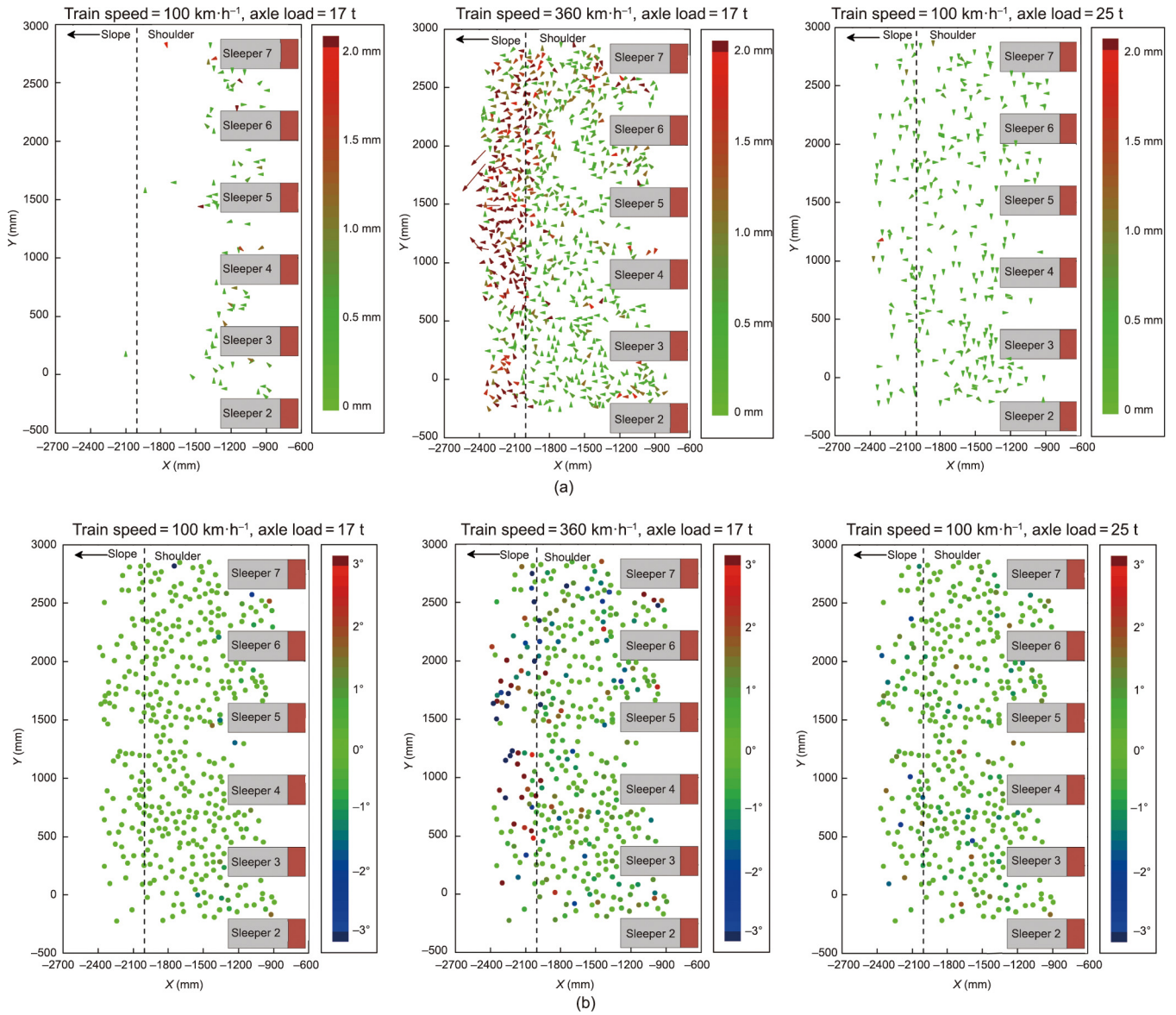
X. Bian, W. Cai, Z. Luo et al.

**Fig. 6.** Movements of surface ballast particles outside sleepers in the dynamic test: (a) displacements and (b) rotation angles.
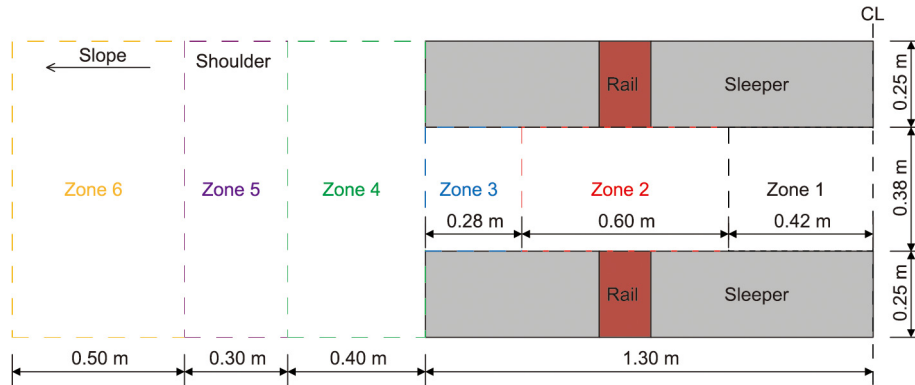


**Fig. 7.** Zone setting of the ballast layer surface. CL: center line.

square meter were approximately 162 and 99, respectively. Thus, the tracked ballast particles were basically uniformly distributed on the horizontal plane.

When the axle load was 17 t, the percentages of moving ballast particles in each zone under the train loads at different speeds are shown in Fig. 9(a). There were generally more moving ballast

X. Bian, W. Cai, Z. Luo et al.
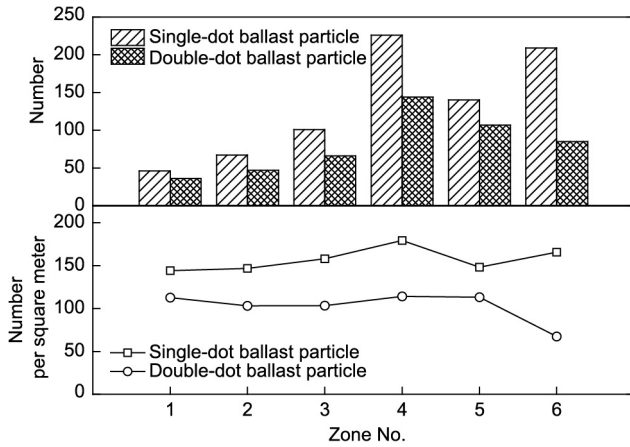
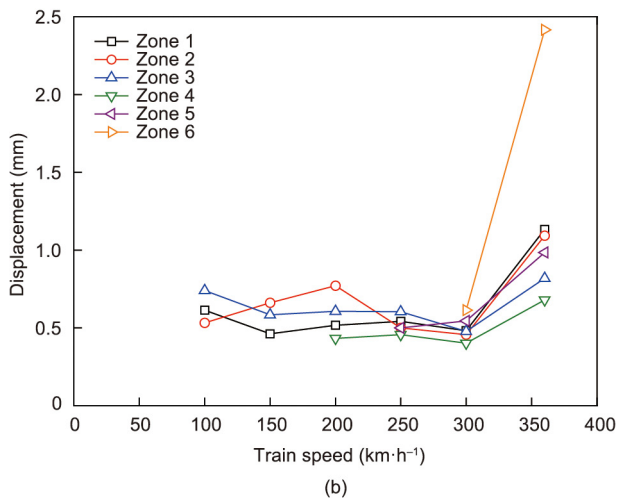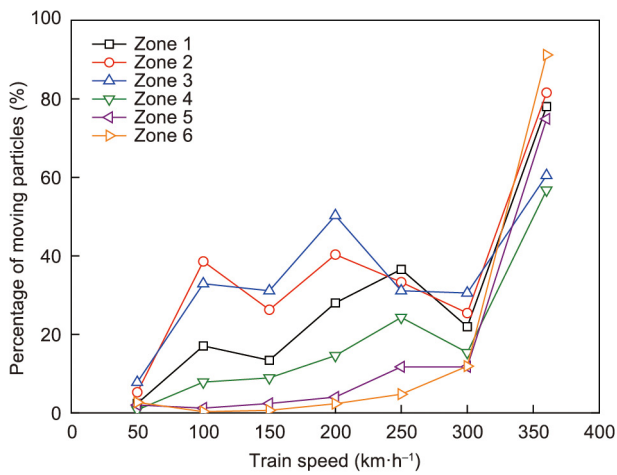**Fig. 8.** Numbers of tracked ballast particles in the specific six zones.



**Fig. 9.** Relationship between surface ballast particle displacement and train speed in the dynamic test (axle load = 17 t): (a) percentages of moving particles and (b) average displacements.

particles in the higher-speed case. Note that there were extremely limited numbers of moving particles as the train speed was low, especially in the zones far from sleepers. To avoid accidental errors, the average displacements were calculated only for those zones with a higher percentage of moving particles than 10%. As shown

in Fig. 9(b), the average displacements showed a trend similar to the percentage of moving particles for various train speeds. As the train speed was lower than 300 km·h$^{-1}$, the ballast particles' average displacements in Zone 2 near the rails and in Zone 3 near the sleeper ends were nearly the largest. Since the train loads were directly applied to the rails so that the vertical sleeper–ballast contact was more effective beneath the rail seat [34] and the horizontal confinement on ballast particles was lower near the sleeper ends than near the sleeper center, the ballast particles in these zones were particularly prone to movement. With the train speed approaching 360 km·h$^{-1}$, the ballast particle displacements in all zones sharply increased, and notably, the average displacement of ballast particles in Zone 6 on the slope reached more than twice those in other zones. It was shown that resonance might occur under high-speed train loads, with the amplitudes and propagation distances of vibration waves greatly increasing, which was likely to cause ballast slope instability. In addition, in comparison between the responses in Zone 1 and those in Zone 3, the ballast particle displacements near the sleeper center grew more rapidly with increasing train speed and then exceeded those near the sleeper ends at a train speed of 360 km·h$^{-1}$. This phenomenon revealed that the resonance of track structures might transform the confinement of adjacent sleepers to excitation for ballast particle displacements between them.

Fig. 10 presents the relationship of the ballast particles' average rotation angle in each zone with the train speed, for a constant 17 t axle load. A comparison between Figs. 9 and 10 revealed no significant difference between the developments of ballast particle displacements and rotations in various loading conditions, suggesting that one of the two movement forms could be estimated by the other.

### 4.1.2. Vibration response of ballast layer

The vertical vibration velocities at different positions of the ballast layer surface were measured by vibration velocity sensors, and then they were differentiated to obtain the vertical vibration accelerations. A comparison with the directly measured accelerations during the dynamic test indicates the reliability of the calculated accelerations from velocities, as shown in Fig. 11. Fig. 12 illustrates the time histories of the applied loads on sleepers and the vertical vibration of the ballast surface at the track center in the high-speed case. The positive sign denotes the downward direction for vibration. As the axle loads approached, the surface ballast particles between two sleepers experienced an upward acceleration owing to the compression and hence gradually rose. This result indicated
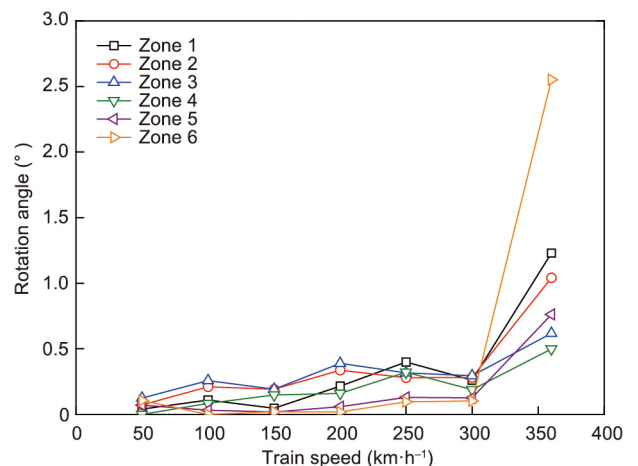


**Fig. 10.** Relationship between surface ballast particle rotation and train speed in the dynamic test (axle load = 17 t).
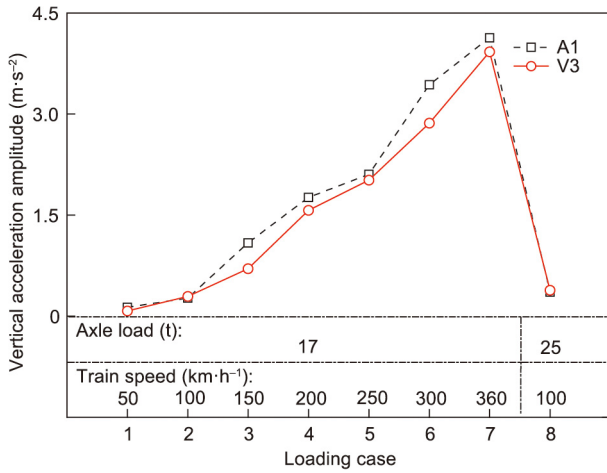
X. Bian, W. Cai, Z. Luo et al.

**Fig. 11.** Comparison of accelerations obtained by acceleration sensor and velocity sensor.

that these ballast particles were partly tossed up. Their acceleration turned downward after the axle loads left, leading to the subsequent fall. As a result, the ballast particles experienced cycles of weightless state and overweight state during the train passage. The contact forces had an important role in the movements of ballast particles, which were linked to their vertical acceleration. If a ballast particle's vertical acceleration equaled the gravity acceleration, the effect of vertical contact forces would disappear, significantly reducing the resistance for the particle movement. It is remarkable that such high vertical accelerations were also reported in previous in situ trials for high-speed railways [35,36], but the relationship between track vibration and ballast particle behavior has rarely been investigated.

The downward acceleration amplitudes of the surface ballast particles under various loading conditions are shown in Fig. 13. It was observed that with an increase in train speed, the vertical acceleration amplitudes across the ballast surface gradually increased. In addition, the vertical acceleration amplitudes were much larger near the track center than at the track edge. Compared

with Figs. 9 and 10, ballast particle flow behavior was shown to be linked to the distribution of vertical acceleration under the train loads. When the train speed was low, the vibration acceleration amplitude peaked under the rail, and the neighboring ballast particle movements were the most dramatic. When the train speed reached or exceeded 300 km·h$^{-1}$, the vibration of the track center was significantly intensified, and the acceleration amplitude here was approximately twice that of the sleeper end, resulting in larger movements of the ballast particles. The vertical acceleration amplitude of the ballast layer approached the gravity acceleration at a train speed of 360 km·h$^{-1}$. In this case, the effective confining pressure of ballast particles might become so small that the stiffness of the ballast layer would be greatly weakened at this instant, and consequently, there would be a great potential for ballast particle flow.

Notably, due to the different surface slopes and surrounding constraints of the track structures, the ballast particle movements would be diverse in the six zones even under the same level of vibration. For example, the ballast particles on the shoulder and slope were more inclined to move than those between two sleepers. Additionally, compared with the influence of the train speed, the variation in acceleration amplitudes caused by increasing axle load was quite trivial, which further explained why ballast particle movements were much less affected by the axle load.

*4.1.3. Particle vibration in ballast layer*

When the train loads were spread inside the ballast layer, the vibration was more complex than that on the surface. The 3D accelerations at the middle depth of the ballast layer were measured by SmartRock sensors, as shown in Fig. 14, in which the lateral, longitudinal, and vertical directions of the railway track were set as the x, y, and z axes, respectively.

When the train speed was less than 200 km·h$^{-1}$, the inside horizontal acceleration amplitudes at different distances from the track center showed no evident variation. With an increase in train speed, the acceleration amplitudes in the X direction became larger in the ballast shoulder than those at the track center due to the significantly growing distance and amplified effect of vibration propagation and relatively low confinement at the track edge. With the exception of a similar surge in the ballast shoulder, the
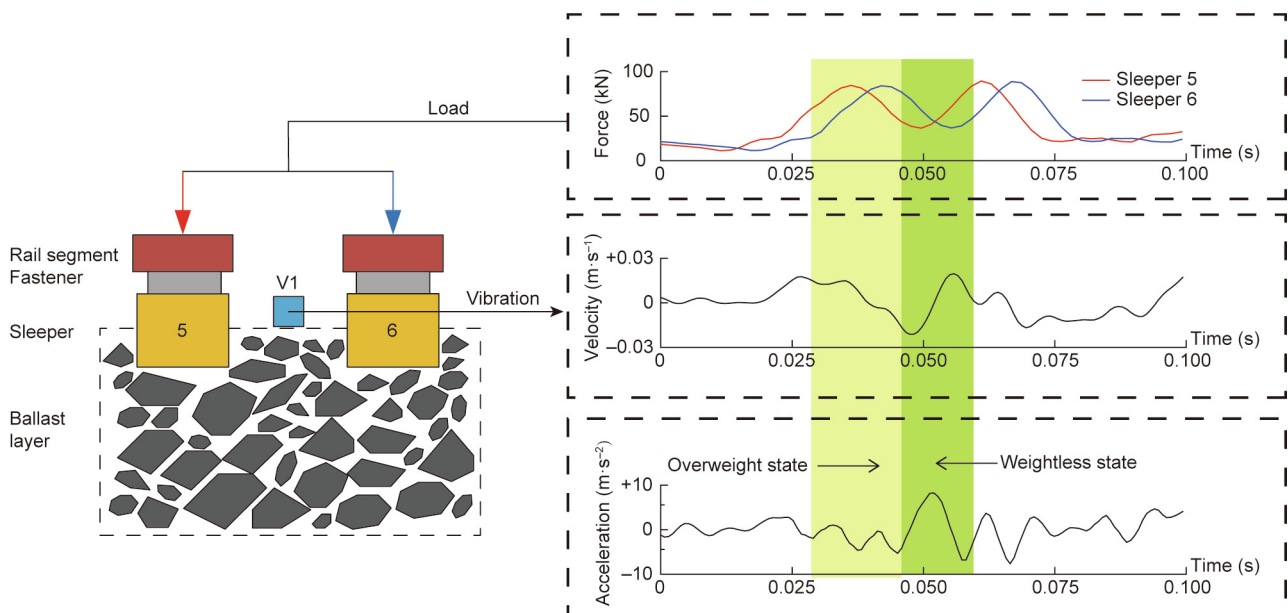


**Fig. 12.** Vibration of ballast surface during the loading process (train speed = 360 km·h$^{-1}$, axle load = 17 t).
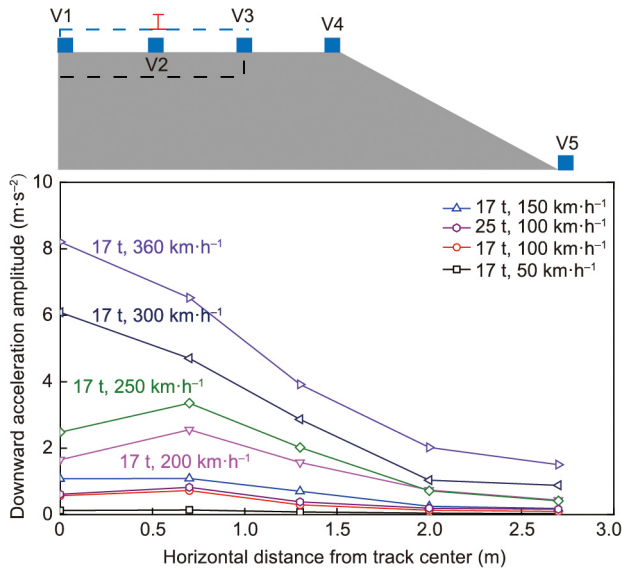
X. Bian, W. Cai, Z. Luo et al.

**Fig. 13.** Distributions of downward acceleration amplitudes on the surface of the ballast layer in the dynamic test.

acceleration amplitudes in the *Y* direction were also greatly amplified with the higher train speed at the track center, which could be explained by the enhanced principal stress rotation under the sleeper center [10,37]. Therefore, when the train speed reached 360 km·h$^{-1}$, the ballast particles at the track edge were subjected to large horizontal forces, and then obvious movements occurred due to the existence of the slope. The relatively moderate lateral acceleration at the track center indicated that the lateral confinement of neighboring ballast particles was considerably weak in the nearly weightless state, which allowed remarkable movements in this direction. Compared Fig. 13 with Fig. 14(c), although the vibration decreased with depth, the vertical acceleration amplitude distributions of the surface and internal ballast particles were similar, reflecting a close relationship between the dynamic responses at both depths. The vibration under the rail was much more violent than that in the ballast shoulder, which accounted for the greater ballast particle movements near the rail. Therefore, the ballast movements near the track center mainly resulted from the vertical vibration, while those at the track edge were mostly caused by the horizontal vibration.

### 4.2. Long-term behavior of ballast layer under train loading

#### 4.2.1. Long-term flow characteristics of ballast particles

The accumulated movements of surface ballasts between sleepers and outside sleepers after long-term loading are shown in Figs. 15 and 16, respectively. As previously mentioned, it was defined that a carriage passed in each loading cycle. Despite the difference in axle loads, the eventual distributions of ballast particle movements after 100 000 cycles of loading from low-speed trains were similar and mainly concentrated near the sleepers. However, when the train speed reached 360 km·h$^{-1}$, many more loading cycles, up to 300 000, were needed to stabilize the track settlement. In this case, the final movements of ballast particles also significantly increased, and the particles with large displacements tended to move outwards. Since the development trends of the ballast particle displacements and rotations were almost consistent in the long-term loading test, the next discussion will mainly focus on the ballast particle displacements for simplicity.

The general developments of the surface ballast particle displacements with loading cycles are shown in Fig. 17, indicating
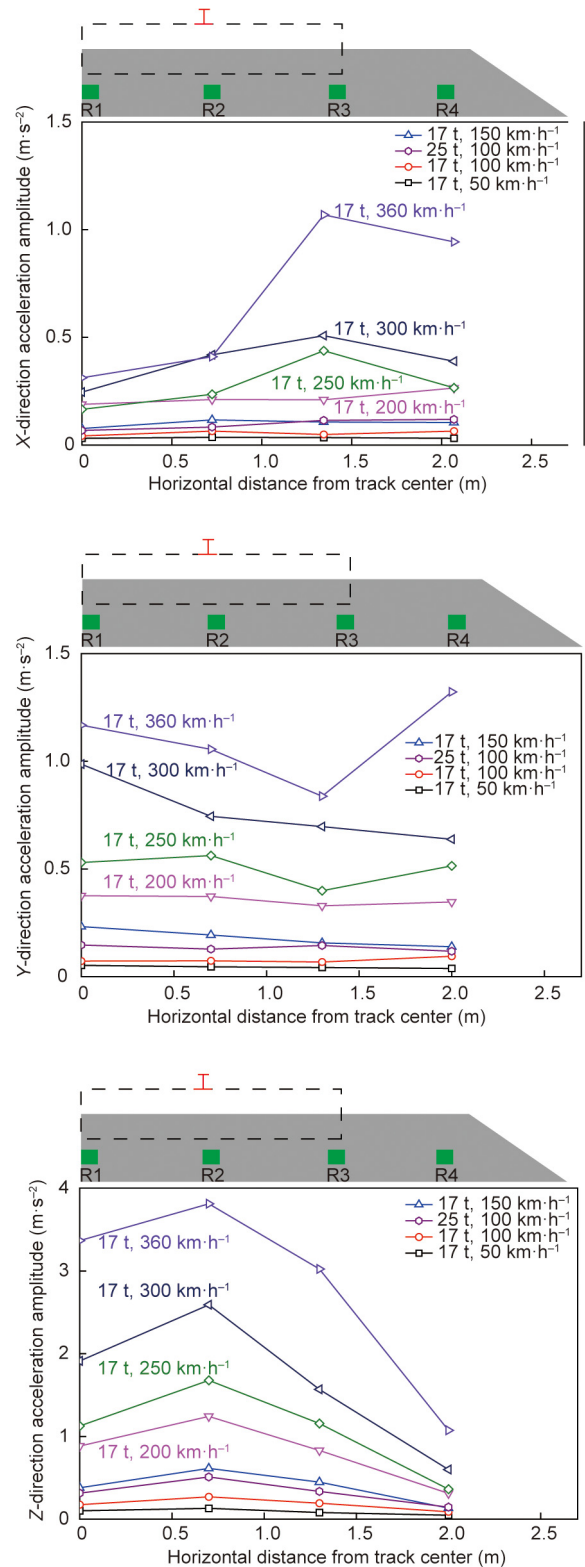


**Fig. 14.** Distributions of acceleration amplitudes at the middle depth of the ballast layer in the dynamic test: (a) *X*-direction; (b) *Y*-direction; and (c) *Z*-direction.

the percentages of the ballast particles that had greater displacements than the selected values. Given the continuous horizontal vibration of ballast particles during the loading process when the photos were taken, especially under high-speed train passage, the fluctuating measured values were treated by introducing
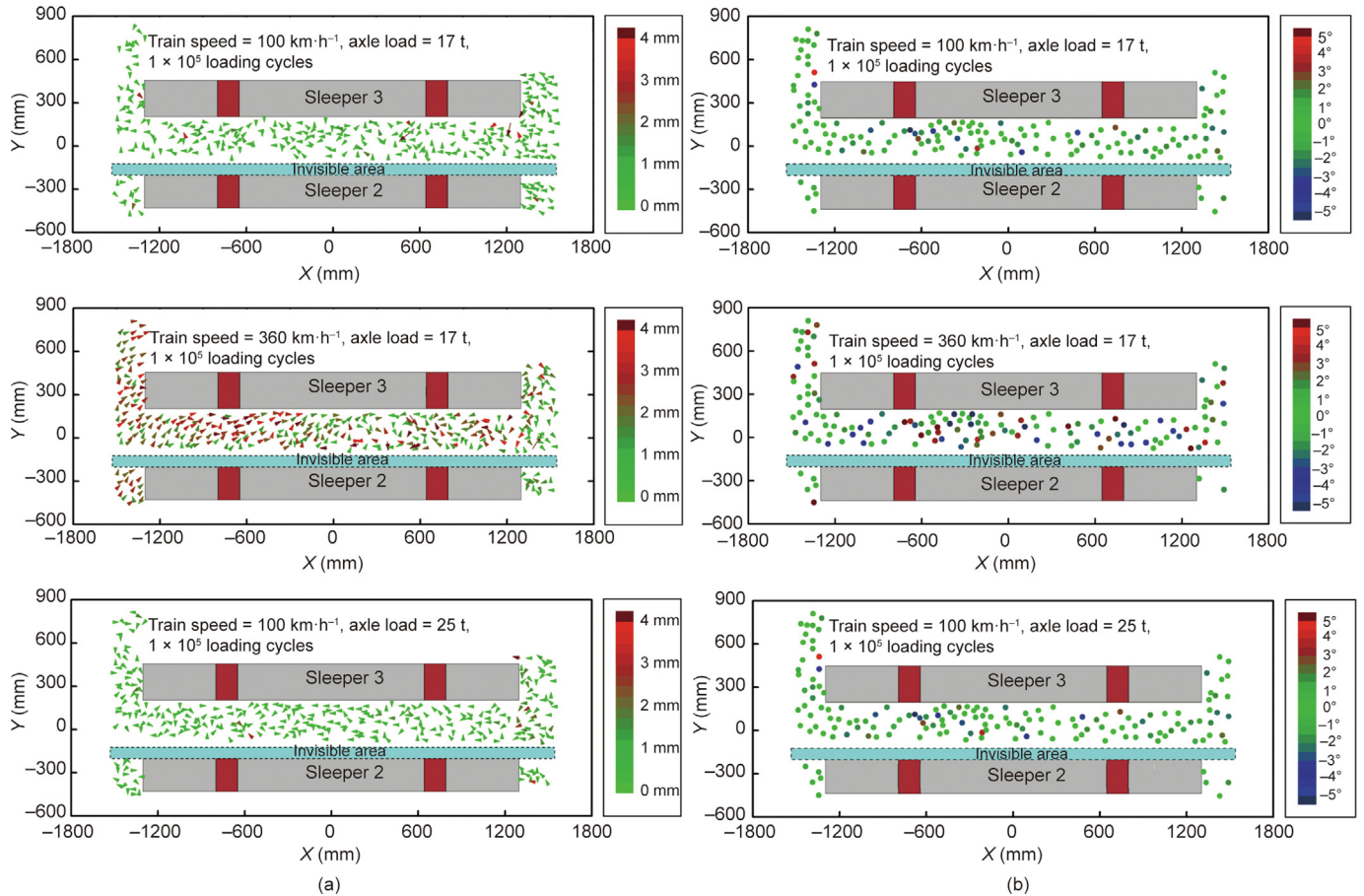
**Fig. 15.** Movements of surface ballast particles between sleepers under the long-term loading: (a) displacements and (b) rotation angles.

smooth curves. The ballast particle displacements rapidly developed, gradually slowed, and then tended to be nearly consistent. The vertical dashed lines between the developing stage and the stable stage in Fig. 17 were determined when the subsequent curves stabilized with fluctuation amplitudes less than 5%. Accordingly, for trains with an axle load of 17 t and a speed of 100 km·h$^{-1}$, trains with an axle load of 17 t and a speed of 360 km·h$^{-1}$, and trains with an axle load of 25 t and a speed of 100 km·h$^{-1}$, the loading cycles needed to reach the stable stages for ballast particle displacements were 50 000, 206 000, and 58 000, respectively; the proportions of ballast particles with final displacements greater than 1 mm were 16%, 67%, and 22%, respectively. Therefore, in the long-term loading test, the influence of train speed on ballast particle displacements was much greater than that of axle load. The high-speed train loads significantly amplified the ballast particle displacements and made them more difficult to stabilize. Since all the loadings were completed in several days and there existed several cycles of loading and unloading processes, the ballast particle movements tended to develop again after certain local stable stages.

The averaged displacements of ballast particles in the $X$ and $Y$ directions in the prescribed zones during long-term loading are shown in Fig. 18. In the case of the low-speed train with small axle loads, it was difficult for the ballast particle displacements in Zone 2 near the rails and Zone 3 near the sleeper ends to stabilize, and their final displacements were larger than those in other places. With the exception of the ballast particles near the track center, which were well restrained by the nearby sleepers, the longitudinal displacements of other ballast particles were slightly larger than the lateral displacements. When the train speed increased

to 360 km·h$^{-1}$, the ballast particles in Zone 6 on the slope had the largest displacements because of numerous particles sliding off the slope, and they continued to move in the subsequent stage of loading, when the ballast particle movements in other zones had become comparatively stable. Due to the significant track settlement caused by high-speed trains, most ballast particles moved laterally away from the sleepers, which was consistent with the experimental results of the model box test by Saussine et al. [19]. Under the heavy haul train passage, the lateral displacements of ballast particles between two sleepers were larger than those outside sleepers, similar to the first loading case, while the longitudinal displacements of ballast particles in Zone 1 near the track center and in Zone 2 near rails were relatively small compared with those far from sleepers. This phenomenon could result from the compaction of ballast particles near the track center due to the previous loading stages, which was likely to mainly restrict their longitudinal movements.

### 4.2.2. Long-term vibration development of ballast layer

The downward acceleration amplitudes at different positions on the ballast layer surface are shown in Fig. 19. Under low-speed train passage, the ballast vibration was gradually weakened to a lower level. The largest acceleration amplitude was kept near rails, which accounted for the evident ballast particle movements here. Under high-speed train loads, the ballast vibration was obviously intensified and then slightly weakened, with final increasing rates of more than 13% in all zones. The downward acceleration amplitudes at the track center approached the gravity acceleration during the loading process, and the consequent complete weightlessness caused the remarkable flow of nearby ballast particles.
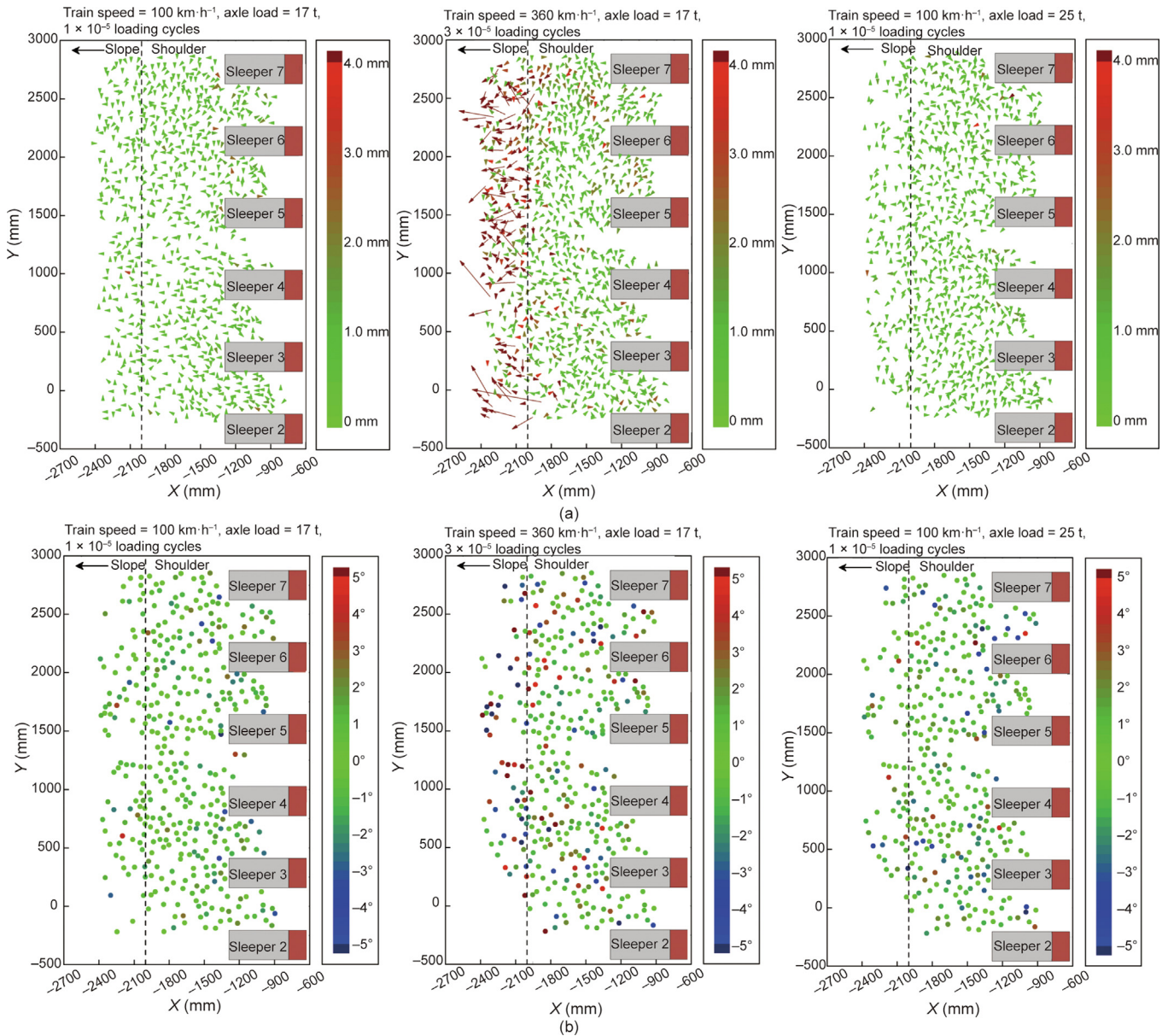
**Fig. 16.** Movements of surface ballast particles outside sleepers under the long-term loading: (a) displacements and (b) rotation angles.

The increase in axle load accelerated the decline of ballast vibration, especially near the track center, which caused the relatively moderate movements of neighboring ballast particles in the long term.

### 4.2.3. Variation in ballasted track performance

The settlement of the sleeper (i.e., settlement of the ballast layer surface) and the settlements of the underlying subballast layer surface and embankment surface, are shown in Fig. 20. When the train speed was low, the sleeper settlement was slight and mainly caused by the movements of ballast particles near the sleepers. Under the high-speed train loading, the sleeper settlement was the largest, approximately 2.5 times those in other loading conditions, and it needed the most loading cycles to reach a steady state. Previous research showed that when the downward acceleration amplitudes of the ballast layer exceeded a critical value, which was related to the gravity acceleration, the development rate of settlement would suddenly increase [38]. In this study, the vibration at the track center, whose downward acceleration could

nearly reach the gravity acceleration, induced significant lateral ballast particle flow, which was the direct reason for the rapid settlement. The ballast particles on the slope and shoulder had obvious lateral movements, providing space for further sleeper settlement. In contrast, the vertical compression of the ballast layer changed from 0.35 mm with an axle load of 17 t to 0.17 mm with an axle load of 25 t, which was likely to be attributed to the significant decline in the longitudinal displacements of ballast particles near the track center. Moreover, a comparison between Figs. 17 and 20 revealed that the development trends of the sleeper settlement with the number of loading cycles were consistent with those of ballast particle movements. By applying the same distinguishing criterion for the stable stage, both the accumulative settlements and ballast particle movements became nearly invariable at almost the same moment in the three long-term loading cases, with relative differences less than 10% in terms of the required loading cycles.

During long-term loading, the static support stiffness of Sleeper 4 was measured, the results are shown in Fig. 21. Under the low-
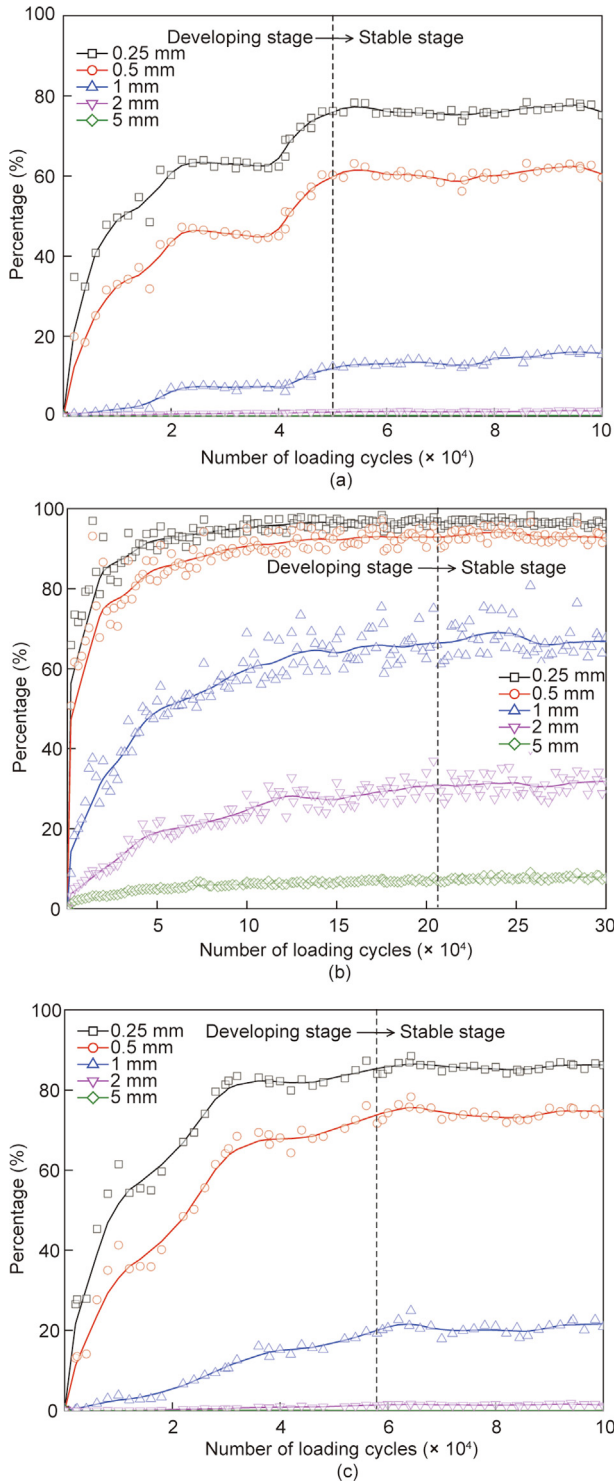
X. Bian, W. Cai, Z. Luo et al.

**Fig. 17.** Percentages of surface ballast particles with larger displacements than certain values under the long-term loading: (a) train speed = 100 km·h$^{-1}$, axle load = 17 t; (b) train speed = 360 km·h$^{-1}$, axle load = 17 t; and (c) train speed = 100 km·h$^{-1}$, axle load = 25 t.



**Fig. 18.** Average *X*-direction and *Y*-direction displacements of surface ballast particles under the long-term loading: (a) train speed = 100 km·h$^{-1}$, axle load = 17 t; (b) train speed = 360 km·h$^{-1}$, axle load = 17 t; and (c) train speed = km·h$^{-1}$, axle load = 25 t.

speed train passage, the sleeper support stiffness gradually increased, which was further intensified by the heavy axle load. However, the high-speed train loads did not significantly strengthen the sleeper support stiffness and even weakened the resilient stiffness for the unloading process. Shi et al. [39] pointed out that the sleeper support stiffness was basically linear with the density of the ballast layer and related to the displacements and
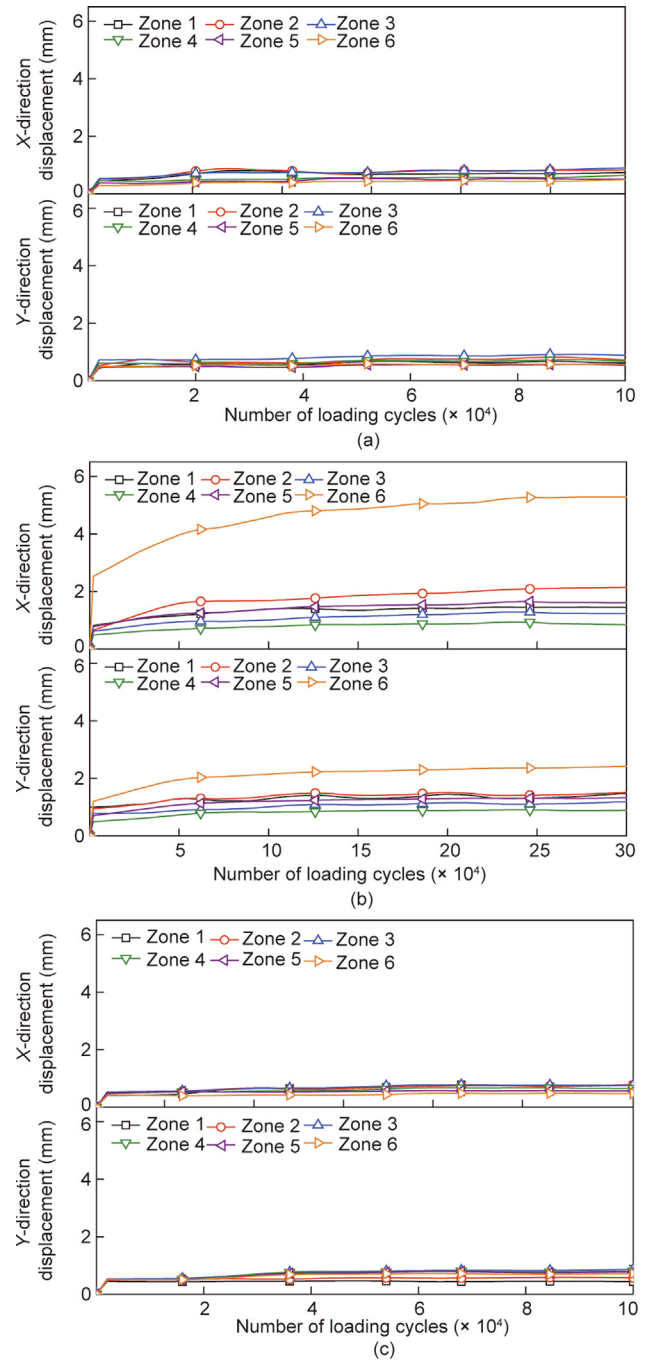
rotations of ballast particles through the discrete-continuous hybrid method. Therefore, when the train speed was low, the lateral displacements of ballast particles were slight, and the track settlement was mainly caused by the compaction and rearrangement of the ballast particles near sleepers, leading to the improvement in sleeper support stiffness. In contrast, as the train speed increased up to 360 km·h$^{-1}$, the track settlement involved the obvious lateral spread of most ballast particles across the whole surface, which could not make the ballast layer denser and hence reduced the sleeper support stiffness.
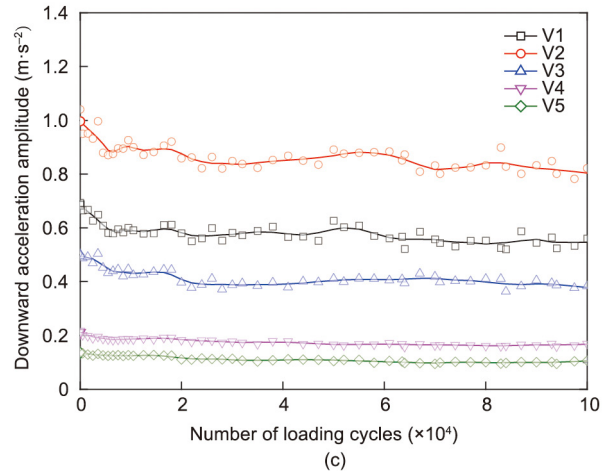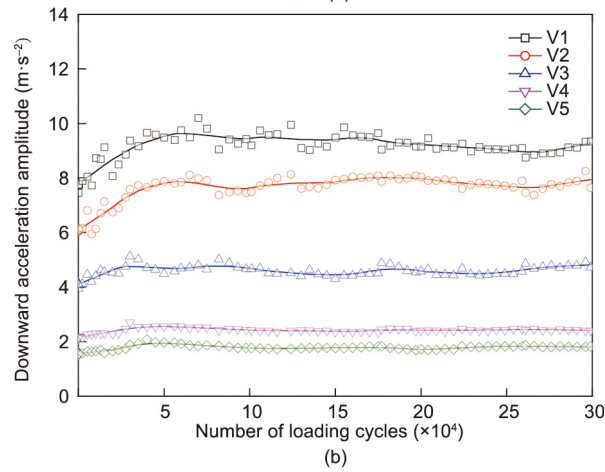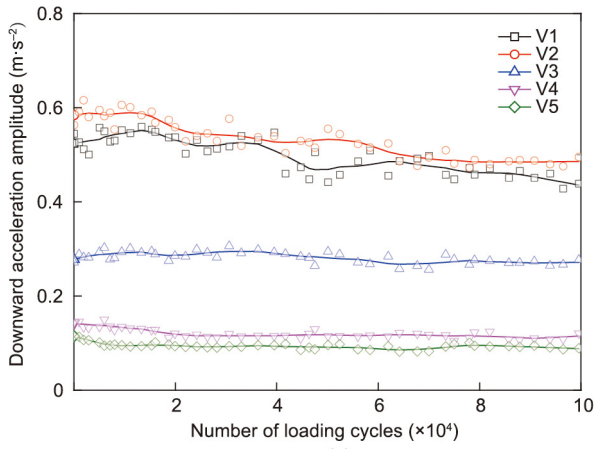
Fig. 19. Downward acceleration amplitudes on the surface of the ballast layer under the long-term loading: (a) train speed = 100 km·h$^{-1}$, axle load = 17 t; (b) train speed = 360 km·h$^{-1}$, axle load = 17 t; and (c) train speed = km·h$^{-1}$, axle load = 25 t.
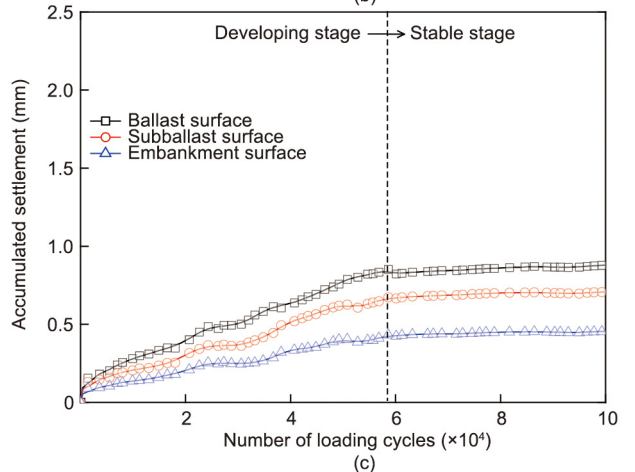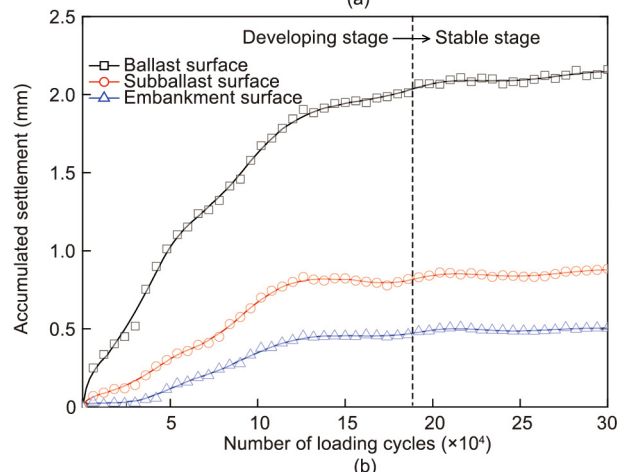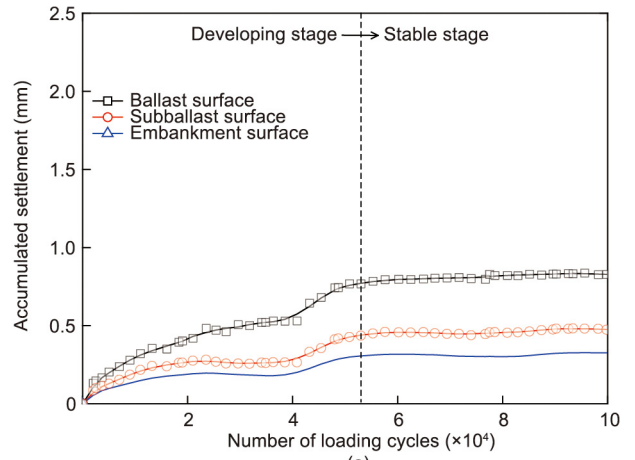


Fig. 20. Accumulated settlements at different depths under the long-term loading: (a) train speed = 100 km·h$^{-1}$, axle load = 17 t; (b) train speed = 360 km·h$^{-1}$, axle load = 17 t; and (c) train speed = 100 km·h$^{-1}$, axle load = 25 t.
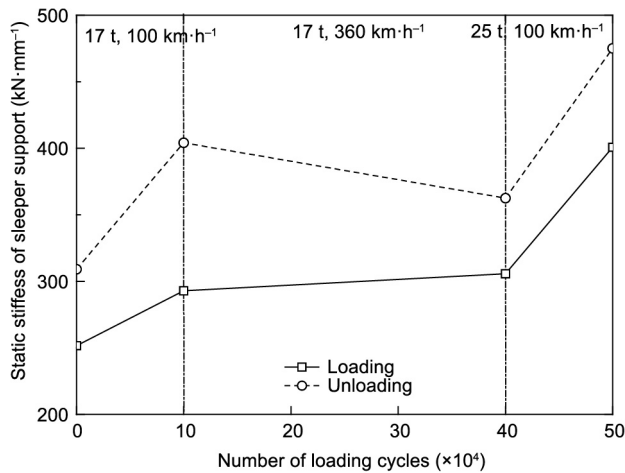
X. Bian, W. Cai, Z. Luo et al.

**Fig. 21.** Development of static stiffnesses of sleeper support during the long-term loading.

## 5. Conclusions

Based on the application of an image-aided technique in a full-scale model test on ballasted tracks, the flow behavior of ballast particles and the performance of ballasted tracks were investigated under various service conditions. The following conclusions can be drawn:

(1) Compared with the train axle load, the train speed had a more significant impact on the surface ballast particle movements. At train speeds lower than 300 km·h$^{-1}$, the moving ballast particles were mainly concentrated near the sleepers. With increasing train speed, the movements of almost all ballast particles were amplified, with many particles sliding down the slope, which would threaten the stability of the track structure.

(2) The vibration of the ballast layer induced by train loads was an important factor contributing to ballast particle movements. As the vertical acceleration of ballast layer was similar to the gravity acceleration, the ballast particles underwent violent movements due to the vanishment of effective constraint by neighboring particles. Specifically, the ballast particle movements near the track center were mainly caused by the vertical vibration, while those on the ballast shoulder and slope were mainly caused by the horizontal vibration.

(3) During the long-term loading test, the movements of ballast particles rapidly developed at the beginning and gradually stabilized with the number of loading cycles, which coincided with the development of track settlement. Both actually influenced each other and simultaneously reached a stable state.

(4) The track settlement and sleeper support stiffness were influenced by the direction and distribution of ballast particle movements during long-term loading. The track settlement was slight, and the sleeper support stiffness increased under the low-speed train loads, which was related to the compaction under sleepers and limited movements of nearby ballast particles. In contrast, the high-speed train loads produced a significant track settlement and reduced sleeper support stiffness due to the notable lateral movements of ballast particles.

The flow behavior of inner ballast particles under the sleeper is also significant for the investigation of track performance. With the exception of the SmartRock sensors embedded in the ballast layer in this study, more refined tests and analyses of the long-term migration of internal ballast particles are needed to further clarify the settlement mechanism under high-speed train loads.

## Compliance with ethics guidelines

Xuecheng Bian, Wenqing Cai, Zheng Luo, Chuang Zhao, and Yunmin Chen declare that they have no conflict of interest or financial conflicts to disclose.

## References

[1] Madshus C, Kaynia AM. High-speed railway lines on soft ground: dynamic behaviour at critical train speed. J Sound Vibr 2000;231(3):689–701.
[2] Lamas-Lopez F, Cui YJ, Calon N, Costa D'Aguiar S, Peixoto De Oliveira M, Zhang TW. Track-bed mechanical behaviour under the impact of train at different speeds. Soil Found 2016;56(4):627–39.
[3] Quinn AD, Hayward M, Baker CJ, Schmid F, Priest JA, Powrie W. A full-scale experimental and modelling study of ballast flight under high-speed trains. Proc Inst Mech Eng, F J Rail Rapid Transit 2010;224(2):61–74.
[4] Selig ET, Waters JM. Track geotechnology and substructure management. London: Thomas Telford; 1994.
[5] Mishra D, Tutumluer E, Boler H, Hyslip JP, Sussmann TR. Railroad track transitions with multidepth deflectometers and strain gauges. Transp Res Rec 2014;2448(1):105–14.
[6] Indraratna B, Nimbalkar S, Christie D, Rujikiatkamjorn C, Vinod J. Field assessment of the performance of a ballasted rail track with and without geosynthetics. J Geotech Geoenviron Eng 2010;136(7):907–17.
[7] Fu LL, Zhou SH, Guo PJ, Tian ZK, Zheng YX. Dynamic characteristics of multiscale longitudinal stress and particle rotation in ballast track under vertical cyclic loads. Acta Geotech 2021;16(5):1527–45.
[8] Chen C, Indraratna B, McDowell G, Rujikiatkamjorn C. Discrete element modelling of lateral displacement of a granular assembly under cyclic loading. Comput Geotech 2015;69:474–84.
[9] Zhang X, Zhao CF, Zhai WM. Dynamic behavior analysis of high-speed railway ballast under moving vehicle loads using discrete element method. Int J Geomech 2017;17(7):04016157.
[10] Bian XC, Li W, Qian Y, Tutumluer E. Analysing the effect of principal stress rotation on railway track settlement by discrete element method. Geotechnique 2020;70(9):803–21.
[11] Guo YL, Markine V, Zhang XH, Qiang WL, Jing GQ. Image analysis for morphology, rheology and degradation study of railway ballast: a review. Transp Geotechnics 2019;18:173–211.
[12] Aikawa A. Determination of dynamic ballast characteristics under transient impact loading. Electron J Struct Eng 2013;13(1):17–34.
[13] Liu SS, Huang H, Qiu T, Gao L. Comparison of laboratory testing using SmartRock and discrete element modeling of ballast particle movement. J Mater Civ Eng 2017;29(3):D6016001.
[14] Fu LL, Tian ZK, Zhou SH, Zheng YX, Wang BL. Characterization of ballast particle's movement associated with loading cycle, magnitude and frequency using SmartRock sensors. Granul Matter 2020;22(3):63.
[15] Pincus HJ, Harris WW, Viggiani G, Mooney MA, Finno RJ. Use of stereophotogrammetry to analyze the development of shear bands in sand. Geotech Test J 1995;18(4):405.
[16] Zhao C, Koseki J, Liu WC. Local deformation behaviour of saturated silica sand during undrained cyclic torsional shear tests using image analysis. Geotechnique 2020;70(7):621–9.
[17] Suits LD, Sheahan TC, Sevi AF, Ge L, Take WA. A large-scale triaxial apparatus for prototype railroad ballast testing. Geotech Test J 2009;32(4):102033.
[18] Ajayi O, Le Pen L, Zervos A, Powrie W. A behavioural framework for fibre-reinforced gravel. Geotechnique 2017;67(1):56–68.
[19] Saussine G, Cholet C, Gautier PE, Dubois F, Bohatier C, Moreau JJ. Modelling ballast behaviour under dynamic loading. Part 1: a 2D polygonal discrete element method approach. Comput Methods Appl Mech Eng 2006;195(19–22):2841–59.
[20] Kumara JJ, Hayano K. Deformation characteristics of fresh and fouled ballasts subjected to tamping maintenance. Soil Found 2016;56(4):652–63.
[21] Guo Y, Jia W, Markine V, Jing G. Rheology study of ballast-sleeper interaction with particle image velocimetry (PIV) and discrete element modelling (DEM). Constr Build Mater 2021;282:122710.
[22] Le Pen L, Bhandari AR, Powrie W. Sleeper end resistance of ballasted railway tracks. J Geotech Geoenviron Eng 2014;140(5):04014004.
[23] Liu H, Xiao JL, Wang P, Liu GZ, Gao MY, Li SZ. Experimental investigation of the characteristics of a granular ballast bed under cyclic longitudinal loading. Constr Build Mater 2018;163:214–24.
[24] Abadi T, Le Pen L, Zervos A, Powrie W. Improving the performance of railway tracks through ballast interventions. Proc Inst Mech Eng, F J Rail Rapid Transit 2018;232(2):337–55.

[25] National Railway Administration of the People's Republic of China. TB 10621–2014: Code for the design of high-speed railway. Chinese standard. Beijing: China Railway Publishing House; 2014. Chinese.

[26] Jiang HG, Bian XC, Cheng C, Chen YM, Chen RP. Simulating train moving loads in physical model testing of railway infrastructure and its numerical calibration. Acta Geotech 2016;11(2):231–42.

[27] American Society for Testing and Materials. ASTM D2487-11: Standard practice for classification of soils for engineering purposes (unified soil classification system). US standard. West Conshohocken: ASTM International; 2011.

[28] Chen RP, Wang YW, Ye XW, Bian XC, Dong XP. Tensile force of geogrids embedded in pile-supported reinforced embankment: a full-scale experimental study. Geotext Geomembr 2016;44(2):157–69.

[29] Li W, Bian XC, Duan X, Tutumluer E. Full-scale model testing on ballasted high-speed railway: dynamic responses and accumulated settlements. Transp Res Rec 2018;2672(10):125–35.

[30] Takemiya H, Bian XC. Substructure simulation of inhomogeneous track and layered ground dynamic interaction under train passage. J Eng Mech 2005;131 (7):699–711.

[31] Bian XC, Jiang HG, Cheng C, Chen YM, Chen RP, Jiang JQ. Full-scale model testing on a ballastless high-speed railway under simulated train moving loads. Soil Dyn Earthquake Eng 2014;66:368–84.

[32] Zhao C, Koseki J, Sasaki T. Image based local deformation measurement of saturated sand specimen in undrained cyclic triaxial tests. Soil Found 2018;58 (6):1313–25.

[33] Zhao C, Koseki J. An image-based method for evaluating local deformations of saturated sand in undrained torsional shear tests. Soil Found 2020;60 (3):608–20.

[34] Abadi T, Le Pen L, Zervos A, Powrie W. Measuring the area and number of ballast particle contacts at sleeper-ballast and ballast-subgrade interfaces. Int J Railw Technol 2015;4(2):45–72.

[35] Chebli H, Clouteau D, Schmitt L. Dynamic response of high-speed ballasted railway tracks: 3D periodic model and in situ measurements. Soil Dyn Earthquake Eng 2008;28(2):118–31.

[36] Ramirez Cardona D, Benkahla J, Costa D'Aguiar S, Calon N, Robinet A, Di Benedetto H, et al. High-speed ballasted track behaviour with sub-ballast bituminous layer. Proceedings of the 2nd International Symposium on Railway Geotechnical Engineering (GeoRail 2014); 2014 Nov 6–7; Paris, France. Paris: Ponts Formation Conseil; 2014.

[37] Varandas JN, Paixao A, Fortunato E, Holscher P. A numerical study on the stress changes in the ballast due to train passages. Procedia Eng 2016;143:1169–76.

[38] Al Shaer A, Duhamel D, Sab K, Foret G, Schmitt L. Experimental settlement and dynamic behavior of a portion of ballasted railway track under high speed trains. J Sound Vibrat 2008;316(1–5):211–33.

[39] Shi C, Zhao CF, Yang Y, Guo YL, Zhang X. Analysis of railway ballasted track stiffness and behavior with a hybrid discrete–continuum approach. Int J Geomech 2021;21(3):04020268.